PNAS Nexus, 2024, 3, pgae470
https://doi.org/10.1093/pnasnexus/pgae470
Advance access publication 17 October 2024
Research Report

Curvature-directed anchoring and defect structure of colloidal smectic liquid crystals in confinement

Ethan I. L. Jull[a,*], Gerardo Campos-Villalobos[a,*], Qianjing Tang[b], Marjolein Dijkstra[a,*] and Lisa Tran[a,*]

[a]Soft Condensed Matter and Biophysics, Debye Institute for Nanomaterials Science, Utrecht University, 3584 CC Utrecht, The Netherlands
[b]Department of Earth Sciences, Utrecht University, 3584 CB Utrecht, The Netherlands
*To whom correspondence should be addressed: Email: e.i.l.jull@uu.nl (E.I.L.J.); g.d.j.camposvillalobos@uu.nl (G.C.-V.); m.dijkstra@uu.nl (M.D.); l.tran@uu.nl (L.T.)
Edited By Peter Fratzl

Abstract

Rod-like objects at high packing fractions can exhibit liquid crystalline ordering. By controlling how the rods align near a boundary, i.e. the anchoring, the defects of a liquid crystal can be selected and tuned. For smectic phases, the rods break rotational and translational symmetry by forming lamellae. Smectic defects thereby include both discontinuities in the rod orientational order (disclinations), as well as in the positional order (dislocations). In this work, we use experiments and simulations to uncover the geometrical conditions necessary for a boundary to set the anchoring of a confined, particle-resolved, smectic liquid crystal. We confine a colloidal smectic within elliptical wells of varying size and shape for a smooth variation of the boundary curvature. We find that the anchoring depends upon the local boundary curvature, with an anchoring transition observed at a critical radius of curvature approximately twice the rod length. Surprisingly, the critical radius of curvature for an anchoring transition holds across a wide range of rod lengths and packing fractions. The anchoring controls the defect structure. By analyzing topological charges and networks composed of maximum density (rod centers) and minimum density (rod ends), we quantify disclinations and dislocations formed with varying confinement geometry. Circular confinements, characterized by planar anchoring, promote disclinations, whereas elliptical confinements, featuring antipodal regions of homeotropic anchoring, promote long-range smectic order and dislocations. Our findings demonstrate how geometrical constraints can control the anchoring and defect structures of liquid crystals—a principle that is applicable from molecular to colloidal length scales.

Keywords: liquid crystals, anchoring, topological defects, smectic, confinement

Significance Statement

Liquid crystals are a prevalent phase of matter found in both synthetic and natural systems. The presence of topological defects dictates the macroscopic behavior of liquid crystals. The conventional technique for manipulating defects in liquid crystals involves the boundary anchoring. For molecules, chemical interactions can set the anchoring angle, but such strategies cannot be applied for nanorods and microrods, which have thus far been limited to planar anchoring. Here, for the first time, we control the perpendicular (homeotropic) anchoring of a confined, colloidal liquid crystal by defining the geometric conditions necessary for an anchoring transition. We demonstrate that the anchoring determines the defect state of a model, colloidal smectic, a phase characterized by density modulation. We show that anchoring influences the defect quantity and type. Our work makes explicit the connection between boundary curvature and anchoring in liquid crystals, a principle that applies across length scales.

Introduction

Topological defects are pervasive in diverse phases of ordered matter, and their presence greatly affects system properties (1). Liquid crystals are prime examples (2), where topological defects in molecular systems facilitate optical applications (3), particle assembly (4–6), and shape transformations in elastomers (7). At the hundreds of nanometer length scale, the liquid crystalline ordering of metal (8) and semiconductor (9) nanorod superlattices tunes their plasmonic resonance (10) and light polarization (9, 11), respectively. At even larger length scales, liquid crystal defects influence biological processes in bacterial biofilm development (12–15), cell proliferation, and morphogenesis (16–21). The allowable defect types are a consequence of the system symmetry. For instance, consider a two-dimensional (2D) nematic liquid crystal where the averaged local orientation of the rod-like molecules is described by the director $\mathbf{n}$ and the angle φ, respectively. The topological charge of a defect, q, can be determined by enclosing the defect in a loop γ and calculating the change in director orientation around the loop, $q = \frac{1}{2\pi}\oint_\gamma \nabla\varphi dl$ (22). Nematic defects exhibit a minimum charge magnitude of $|q| = \frac{1}{2}$, reflecting the head–tail

Competing Interest: The authors declare no competing interests.
Received: September 20, 2024. **Accepted:** October 4, 2024

symmetry of their rod-like components. These defects, known as disclinations, manifest as localized regions that violate orientational order (22, 23). In more intricate smectic liquid crystals, translational symmetry is broken through the formation of lamellae, introducing a density modulation on top of orientational order. Consequently, smectics accommodate both disclinations and dislocations, which are defects in the density periodicity (22, 24). The ability to control defects in more complex liquid crystal phases is essential for their application in nano- and bio-technologies (9, 25–30).

Interest in smectics has been recently renewed due to advances in experimental techniques (31–40), topological classification (41–47), and continuum modeling (48–51). Defects in molecular smectics have been stabilized with topological and geometrical constraints, but analyses have predominantly relied on mesoscopic modeling of the elastic energy F (31–33, 35–37), given by:

$$F = \int dV \left\{ \frac{B}{2}\left[\frac{\partial u}{\partial z} - \frac{1}{2}\left(\frac{\partial u}{\partial x}\right)^2\right]^2 + \frac{K}{2}\left(\frac{\partial^2 u}{\partial x^2}\right)^2 \right\}, \quad (1)$$

where V is the volume, $u(x, z)$ is the displacement of the smectic lamellae, and B and K are the layer compression and the layer bending moduli, respectively (2). In the colloidal domain, theoretical efforts focused primarily on microscopic, classical density functional theory, and Monte Carlo (MC) simulations to map out smectic order in phase diagrams of hard rods (52–56). The phase diagrams have been probed experimentally with suspensions of rod-like viruses (57, 58) and silica particles (34, 59). Only in the past year has microscopic theory been connected to smectic elasticity (Eq. 1) (51). Similarly, researchers have recently started exploring smectic defects from a microscopic viewpoint. Using simulations and experiments, colloidal smectics have been confined within various geometries, such as rectangles (38, 60, 61), hexagons (44), circles (62–64), and annuli (64–66), establishing a correlation between the confining geometry and the types of defects formed. The defects were found to adhere to global, topological constraints (44, 46, 64, 66). Yet, these colloidal systems are constrained in their possible defect configurations due to the lack of control over *homeotropic anchoring* of liquid crystals at length scales larger than that of molecules (38, 67).

Anchoring, which describes the average rod alignment at a boundary (68), is essential for the manipulation of topological defects in liquid crystals. Directing the rod anchoring to be either tangent to the boundary (planar anchoring) or perpendicular to it (homeotropic anchoring) influences the configuration and types of defects produced within a confined system. Thus far, full control of the rod anchoring has been limited to molecular systems. For small, liquid crystal molecules, the anchoring can be selected by choosing the appropriate surface chemistry, but these methods are not applicable to systems consisting of nanometer- to micrometer-sized particles. Since particle-based models rely predominantly on entropic interactions, only the geometry of the confining boundary can be tuned. In simulations and classical density functional theory frameworks, altering the entropic interactions of a particle with a wall has been shown to select a specific anchoring type (69–74). Planar anchoring at surfaces is commonly observed (38, 64, 75–77). However, control over the homeotropic anchoring of confined hard rods has still not been achieved in experimental systems (38, 69, 70, 72, 73). Realizing homeotropic anchoring solely from entropic interactions remains an ongoing challenge that must be addressed to effectively design liquid crystal defects in systems of particles (38, 78), crucial for directing the macroscopic properties of confined nanorod superlattices (9–11), and biological systems (16–21).

Here, using a combination of experiments and simulations, we successfully achieve anchoring control in a model system: a 2D, colloidal smectic confined within ellipses of varying sizes and eccentricities. We use this model confinement geometry, which is topologically required to form defects, in order to demonstrate that anchoring control directs the type and composition of defects formed. The ellipse geometry allows for a gradual variation of the local curvature, such that the critical curvature for anchoring transitions can be identified. Experimentally, we synthesize colloidal silica rods with fluorescently labeled shells (Fig. 1A and B), which enable single-particle tracking of each rod using fluorescence confocal microscopy. We confine the silica rods by sedimentation into elliptical wells fabricated with photolithography (Fig. 1C, top). The local confinement curvature is set by the system size, measured by the ratio of the ellipse short-axis radius to the rod length (r_1/L), as well as the system shape, adjusted by r_1/r_2, the ratio of minor to major axes of the ellipse, respectively (Fig. 1C, bottom). The ratio r_1/r_2 determines the eccentricity e of a conic section, defined as $e^2 = 1 - (r_1/r_2)^2$, which, for an ellipse, takes on values between 0 (circular) and 1 (highly elliptical). The confinement size r_1/L is varied from 0.6 to 5.9, and the confinement shape is varied with r_1/r_2 ranging from 0.2 to 1.0. In our MC simulations, we model the system using a 2D, monodisperse system of hard "discorectangles" (Fig. 1D, bottom). Working with an end-to-end, length-to-diameter ratio of ∼8, we study a smectic phase at packing fractions that exhibit meta-stable and short-range, quasi-tetratic order—local regions with fourfold rotational symmetry. To analyze these structures, we examine nematic and tetratic order parameters, along with an analysis of networks consisting of minimum and maximum density points. We identify network features and, for first time, leverage network loops to unambiguously distinguish disclinations, (edge) dislocations, and tetratic order. Both in simulations and experiments (Fig. 1D), we find that anchoring control from highly elliptical confinements stabilizes the smectic phase and induces dislocations. On the other hand, more circular confinements give rise to disclinations and tetratic order. Interestingly, differences in the number and types of defects between experiments and simulations point to variations in the smectic elasticity due to the presence of polydispersity in the rod size. With this work, we demonstrate anchoring control of a colloidal smectic, broadening the tunability of defect states in larger-scaled, liquid crystal systems.

Materials and methods

Experimental methods

In our experiments, we use fluorescently labeled silica rods that are imaged using high-resolution, confocal laser scanning microscopy (Fig. 1A and B). Details of the synthesis can be found in Supplementary Material. Notably, each rod is labeled by a shell of fluorescent molecules, enabling single-particle tracking of each rod position and orientation, as well as particle-resolved characterization of smectic defects. To reduce the polydispersity of the obtained rods, the suspension was cleaned via centrifugation (see Supplementary Material). Our fluorescently-labeled silica rods have an average length of $L = 8.6 \pm 0.1\,\mu$m and diameter of $D = 1.16 \pm 0.02\,\mu$m, with polydispersities of 13% and 20%, respectively (Fig. 1B). Averaging over the length-to-diameter ratios of each measured rod gives $L/D = 7.7 \pm 0.1$ (Fig. 1A). The rod length-to-diameter ratio used in our study is smaller than those used in previous investigations (38, 44, 63–66) and gives rise to additional metastable structures beyond smectic layering.

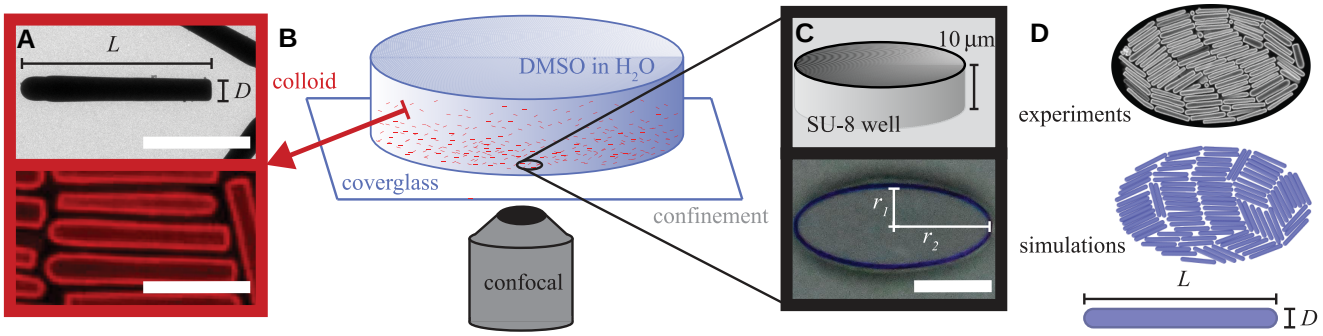

Fig. 1. A) Transmission electron (top) and fluorescence confocal (bottom) micrographs of synthesized colloidal silica rods, with length $L = 8.6 \pm 0.1\,\mu$m and diameter $D = 1.16 \pm 0.02\,\mu$m. Scale bars are 5 μm. B) Schematic of experimental setup depicting the glass container filled with silica rods suspended in 91 wt.-% DMSO-in-water. The confinement wells are on the bottom coverglass, and the rods are sedimented into the wells. C) Schematic and micrograph of an elliptical confinement with $r_1/r_2 = 0.4$, $r_1/L = 3.0$, made of SU-8 photoresist with a height of 10 μm. Scale bar is 50 μm. D) Example experiment and simulation snapshots.

To form a colloidal smectic, we concentrate the rods at the bottom of our samples via sedimentation. We note that confinement can alter the packing fraction at equilibrium compared to unconfined systems (Supplementary Material). The measured rod packing fraction ϕ in experiments varies between 0.60 and 0.85 across all confinement geometries. For larger confinements that can fit more than four smectic layers across the short ellipse axis ($2r_1$), we measure $0.67 \leq \phi \leq 0.85$, with errors in ϕ ranging from 0.03–0.08 across samples due to inaccuracies in particle tracking. With smectic ordering expected at $\phi \approx 0.75$ for our rod aspect ratios of $L/D \approx 8$ (79), our confined rods are, within error, at packing fractions where smectic ordering with metastable tetratic ordering is expected.

To match the refractive index of silica microparticles (~ 1.45), the rods are sedimented in 91 wt.-% dimethylsulfoxide (DMSO, Sigma-Aldrich) in water, allowing for high-resolution confocal microscopy and single-particle analysis (Fig. 1B). At the bottom of the samples are confining wells (Fig. 1C) fabricated on #1 cover glass (130-170 μm thickness, VWR) using contact photolithography (see Supplementary Material).

To alter the local curvature, we vary our elliptical confinements by changing their relative size and shape. The global curvature of the confinement is kept fixed and is described by the Euler characteristic (χ). Following the Poincaré–Hopf theorem, the total topological charge q is conserved, with $\sum q = \chi = +1$ (87, 88).

Computational methods

In our computational approach, we consider 2D monodisperse systems of rods modeled as hard spherocylinders of end-to-end, length-to-diameter ratio $L/D = 8$ (Fig. 1D, bottom). As the particles are confined to lie in a plane, they can be more precisely described as "discorectangles," defined as a rectangle of length $L - D$ and width D capped at each end by a semicircle of diameter D. The bulk phase behavior is studied using constant pressure (NPT) MC simulations under periodic boundary conditions. The equation of state is obtained from compression of an isotropic phase and expansion of a perfect smectic-like phase, using $N = 1{,}000$ and $N = 996$ particles, respectively.

To mimic the experiments, we perform MC simulations of particles confined within various 2D elliptical boundaries. Particles are forced to reside within the elliptical regions by assuming a purely hard interaction with the external walls, thereby favoring planar surface anchoring. As we are interested in smectic-like structures to match experimental observations, we choose to fix the area fraction of the confined particles at $\phi = NA_p/A = 0.81$, with $A_p = (L - D)D + \pi D^2/4$, the area of a hard particle and $A = \pi r_1 r_2$, the area of the confining elliptical geometry. To obtain the desired value of $\phi = 0.81$, where the smectic phase is stable in bulk, we slowly compress a low-density configuration with $\phi \ll 1$, initially placed in a scaled confining geometry.

To speed up the equilibration of the MC simulations, we implement, in addition to simple particle translation and rotation moves, MC moves in which square clusters of particles of dimensions approximately equal to the length of a single particle, are rotated by $\pm 90°$. All simulations are run for at least 2.5×10^7 cycles. We sample equilibrium configurations in the canonical ensemble at constant temperature, number of particles, and confinement area. Unless stated otherwise, all the average quantities are measured over 1,000 configurations selected from the last 10^6 MC cycles. We then compare computational and experimental results for each system size and eccentricity (Fig. 1D).

Results and Discussion

Confinement and anchoring

To examine the influence of confinement on smectic ordering in a smectic that exhibits metastable structures, we use rods with an aspect ratio of $L/D = 8$ in simulations and $L/D = 7.7 \pm 0.1$ in experiments. Simulations by Bates and Frenkel predicted the formation of a smectic phase in 2D rods with an end-to-end length-to-diameter ratio of $L/D \sim 8$ at packing fractions $\phi \geq 0.75$ (79). Yet, there are subtleties in the pathways taken to form the smectic phase. The isotropic-to-smectic transition is not preceded by a uniaxial nematic state, hindering direct nucleation of a smectic phase through compression from an isotropic phase (79, 80). Instead, (short-ranged) metastable tetratic order is commonly observed (63, 79, 80). Bates and Frenkel find that even in simulations incorporating stack-rotation moves, a single-domain smectic phase can only be achieved by *expansion* to $\phi = 0.75$ from a well-ordered and fully aligned crystal. Using rods with low aspect ratios $L/D \sim 8$, we observe metastable, tetratic order in both our experiments and simulations, detailed in Supplementary Material, Fig. S1, and Video S1.

To quantify the nematic and tetratic order in our system, we employ the 2D local orientational order parameter $P_m(\mathbf{r}) = |\langle \exp(im\theta_j) \rangle_{\mathbf{r}}|$, with θ_j the angle formed by the orientation vector of the jth particle ($\hat{\mathbf{u}}_j = (\cos\theta_j,\ \sin\theta_j)^{\mathrm{T}}$) with respect to an arbitrary fixed axis, the angular brackets $\langle \cdots \rangle_{\mathbf{r}}$ denote an average over all particles intersecting a local circle around $\mathbf{r}$ with radius $r_c = 4D$, and m is an integer (44). For $m = 2$, $P_2(\mathbf{r})$ measures the

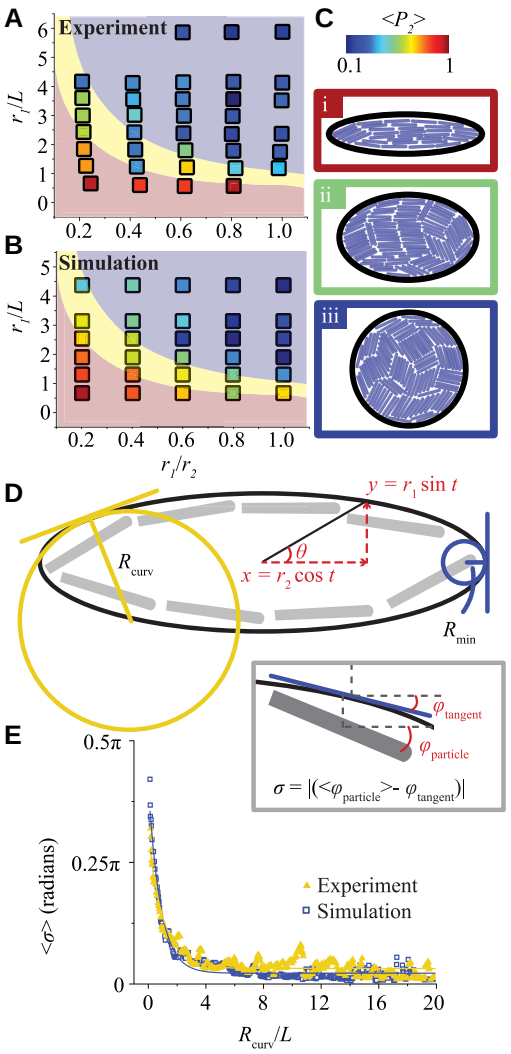

Fig. 2. Global nematic order parameter $\langle P_2 \rangle$ plotted for varying confinement shape r_1/r_2 and size r_1/L for both A) experiments and B) simulations. The background colors denote different regimes, characterized by the smallest value of the radius of curvature R_{min} for a given ellipse, where red is $R_{min}/L \leq 0.5$, yellow is $0.5 < R_{min}/L \leq 1$, and blue is $R_{min}/L > 1$. C) Simulation snapshots are shown on the right for confinement parameters of i) $r_1/r_2 = 0.2$, $r_1/L = 0.6$, ii) $r_1/r_2 = 0.6$, $r_1/L = 1.7$, and iii) $r_1/r_2 = 1.0$, $r_1/L = 2.3$. The box color of each snapshot reflects the $\langle P_2 \rangle$ value, which are: i) 0.96, ii) 0.53, and iii) 0.16. D) The radius of curvature R_{curv} varies around an ellipse perimeter. Example radii of curvature at two different points on the ellipse boundary are drawn here with the associated tangent line at each point. The radius of curvature is given by Eq. 2. The Cartesian axes are labeled in red, with the eccentric angle θ given by $\theta = \tan^{-1}(r_1/r_2 \tan t)$, where t is the polar angle. E) The average deviation $\langle \sigma \rangle$ of the average particle orientation $\langle \varphi_{particle} \rangle$ from the boundary tangent angle $\varphi_{tangent}$ (inset), is plotted as a function of R_{curv}/L. A transition from homeotropic (perpendicular) to planar (tangential) anchoring is observed with increasing R_{curv}/L. Both experimental (yellow triangles) and simulated data points (blue squares) are fitted to exponential decays.

degree of local nematic order. $P_m(\mathbf{r})$ takes values $\in [0, 1]$, where 0 and 1 indicate low and high orientational order around $\mathbf{r}$, respectively. We additionally calculate the global order parameter of the system $\langle P_m \rangle$ by determining the order parameter over the entire system area. We use global order parameter values to characterize the degree of order in the system, while local order parameter values are used to identify disclinations.

At $\phi \approx 0.75$, in both experiments and simulations, confinement starts to influence the bulk ordering, depending upon the confinement shape and size. In Fig. 2, $\langle P_2 \rangle$ is plotted as a function of the system shape r_1/r_2 and size r_1/L. A reduction in $\langle P_2 \rangle$ is observed when moving from the bottom left region, low value of r_1/r_2 and small system size, to the top right, high value of r_1/r_2 and large system size. Generally, a decrease in r_1/r_2, i.e. an increase in confinement eccentricity, leads to higher $\langle P_2 \rangle$ values, indicating increased orientational order arising from well-aligned, smectic layers.

We attribute the increased smectic order with higher confinement eccentricity to the change in rod anchoring from planar to homeotropic near the ellipse vertices. The equation describing an ellipse boundary is given by $x = r_2 \cos t$, $y = r_1 \sin t$, where x and y are Cartesian coordinates, and t is the polar angle, which varies from 0 to 2π. The radius of curvature, R_{curv}, for an ellipse varies around the perimeter, as illustrated in Fig. 2D, and is given by:

$$R_{curv}(t) = \frac{(r_1^2 \cos^2 t + r_2^2 \sin^2 t)^{3/2}}{r_1 r_2}. \quad (2)$$

We define the smallest value of R_{curv} for a given ellipse shape as R_{min}, located at the ellipse vertices and focus on how $\langle P_2 \rangle$ varies with R_{min}. For $R_{min}/L \leq 0.5$ (red regions in Fig. 2), we observe homeotropic anchoring at the ellipse ends, shown in Fig. 2C-i. This homeotropic anchoring results in a single smectic domain, characterized by a high $\langle P_2 \rangle$ value of ≥ 0.7. As we move towards intermediate R_{min} values, ($0.5 < R_{min}/L \leq 1$, yellow regions in Fig. 2), we observe a reduction in $\langle P_2 \rangle$ from ~ 0.7 to ~ 0.5. We attribute this reduction in $\langle P_2 \rangle$ to an increase in the proportion of rods tilting away from the boundary normal at the ellipse vertices, as depicted in Fig. 2C-ii. Lastly, for confinements with $R_{min}/L > 1$ (blue regions in Fig. 2), we find a relatively uniform distribution of rod orientations, resulting in $\langle P_2 \rangle \leq 0.4$. An example is shown in Fig. 2C-iii. We ascribe the lower orientational order in the system to the predominantly planar anchoring around the confinement boundary. We note that in circular confinements, regions of uncontrolled homeotropic anchoring can occur due to adsorbed regions of tetratic ordering to the boundary, as observable in Fig. 2C-iii. Generally, R_{min} decreases below some critical value beyond which an anchoring transition from homeotropic to planar occurs.

To identify the critical radius of curvature R^*_{curv} for an anchoring transition to arise, we analyze the average particle orientation at the boundary for all confinement geometries. The deviation of the average rod orientation angle $\langle \varphi_{particle} \rangle$ from the tangential angle $\varphi_{tangent}$ of the boundary (see inset in Fig. 2D) is calculated around the perimeter of the ellipse for each confinement. At each point around the perimeter, we draw a circle with a radius twice the rod diameter $2D$ and average the rod orientation weighted by the area of each rod that is enclosed within the circle, to determine $\langle \varphi_{particle} \rangle$. Additionally, we calculate R_{curv} at each increment using Eq. 2. The angle deviation $\sigma = |(\langle \varphi_{particle} \rangle - \varphi_{tangent})|$ is binned and then averaged as a function of R_{curv}/L across all confinement samples, as plotted in Fig. 2E. Additional details can be found in Supplementary Material and Fig. S2. We fit the average angle deviation $\langle \sigma \rangle$ as a function of R_{curv}/L to an exponential decay, finding $\langle \sigma \rangle \approx (0.27)\exp[-0.93(R_{curv}/L)] + 0.03$ for experiments and $\langle \sigma \rangle \approx (0.38)\exp[-1.18(R_{curv}/L)] + 0.02$ for simulations. Defining planar anchoring as a rod orientation ± 15 degrees from the tangent ($\langle \sigma \rangle = 0.08\pi$), we find the critical radius of curvature $R^*_{curv}/L \approx 1.9$ for experiments and $R^*_{curv}/L \approx 1.6$ for simulations. We note that the noise of $\langle \sigma \rangle$ beyond $R^*_{curv}/L \sim 2$ is due to the occasional adsorbed region of tetratic ordering to the boundary, seen also in

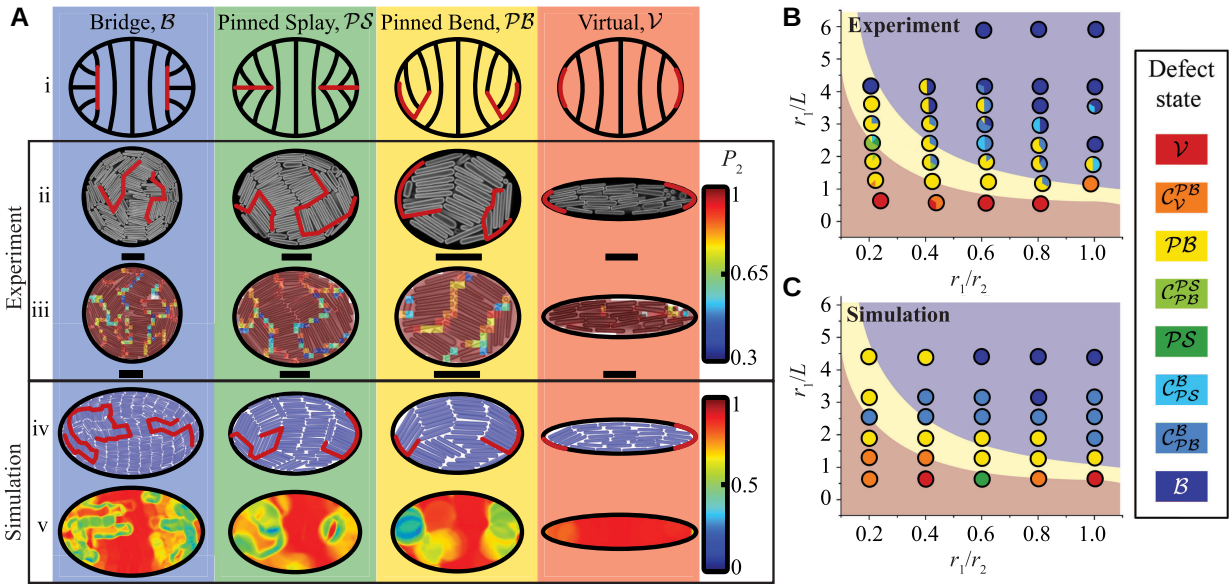

Fig. 3. A) Bridge ($\mathcal{B}$), pinned splay ($\mathcal{PS}$), pinned bend ($\mathcal{PB}$), and virtual ($\mathcal{V}$) disclination states observed for varying confinements. i) Idealized structures are shown with black lines representing smectic layers and red lines representing disclinations. Experiment ii) snapshots and iii) local P_2 mapping (see color bars) are shown (scale bars are 10μm). Simulation iv) snapshots and v) local P_2 mapping are also shown. Disclination states are plotted for varying confinement size (r_1/L) and shape (r_1/r_2), for both B) experiments and C) simulations. A transition from the $\mathcal{V}$ to the $\mathcal{B}$ state is observed with increasing confinement size and decreasing eccentricity (i.e. increasing r_1/r_2), passing through intermediate $\mathcal{PB}$, $\mathcal{PS}$, and composite states. The background colors again denote different regimes, characterized by the smallest value of the radii of curvature R_{min}/L for a given ellipse, where red is $R_{min}/L \leq 0.5$, yellow is $0.5 < R_{min}/L \leq 1$, and blue is $R_{min}/L > 1$. The R_{min}/L regimes demarcate the shifts in disclination states, indicating a relationship between the curvature-imposed anchoring and the disclination state.

Fig. 2C. Generally, these regions are outliers in the overall anchoring behavior of rods, reflected by the low value of the noise compared to definitive homeotropic anchoring below $R^*_{curv} \sim 2$ (see also Fig. S3.)

The critical radius of curvature R^*_{curv} being approximately twice the rod length L suggests that the excluded area of the rods changes with boundary curvature. As curvature varies, the rods alter their orientation relative to the boundary to achieve a more efficient packing. Instead of packing end-to-end as in planar anchoring, more rods can occupy the area near the boundary by stacking side-to-side, resulting in homeotropic anchoring. The tradeoff between minimizing the rod-boundary excluded area and the excluded area with neighboring rods appears to occur at a radius of curvature between L and $2L$. To probe the robustness of our result, we measure R^*_{curv} in simulations of rods with $L/D = 5$, 8, 11, and 14, confined within ellipses and for varying packing fractions ϕ to access both nematic and smectic phases. The angle deviation σ for each parameter is plotted against R_{curv}/L in Fig. S3. Surprisingly, we find that all systems yield $R^*_{curv} \approx 2L$, regardless of whether the system is nematic or smectic (see Fig. S3 and Table S1). Our findings show that boundary curvature plays a crucial role in determining the anchoring condition for hard rods, with a robust critical radius of curvature yielding a homeotropic anchoring transition, irrespective of rod aspect ratio and packing fraction.

Smectic disclination structure

After establishing that local boundary curvature determines the anchoring of confined hard rods, we now demonstrate that entropic anchoring can control the disclination structure of a model smectic formed by rods with $L/D \approx 8$. The defects in the system are influenced by both the local curvature of the confinement (the size and eccentricity) as well as its global curvature (fixed Euler characteristic $\chi = +1$, which is a topological quantity that is invariant to smooth deformations). We first identify disclinations in experiments and simulations by mapping the local nematic order parameter P_2 (Fig. 3A). Local P_2 values can be used to identify disclinations. Our MC simulations run for at least 2.5×10^7 cycles, while our experiments are observed periodically over a period ranging from 1 to 5 months. In analyzing the smectic layer conformation, we ignore interstitials—single rods that orient parallel to the layers and are located in between them (54). Across varying confinement sizes and shapes, the observed disclination configurations can be categorized by four states that we identify as the bridge ($\mathcal{B}$), pinned splay ($\mathcal{PS}$), pinned bend ($\mathcal{PB}$), and virtual ($\mathcal{V}$) states.

Starting at large confinement dimensions with low eccentricity ($r_1/L \geq 2.4, r_1/r_2 \geq 0.6$), the $\mathcal{B}$ state is observed. This state is characterized by two antipodal disclinations, disconnected from the boundary, typically with a large central smectic domain (44, 64). Disclinations are labeled by red lines in Fig. 3A, and for the bridge state, the red disclination lines are entirely within the bulk. Planar anchoring is maintained around the confinement boundary.

For intermediate confinement sizes ($1.2 \leq r_1/L \leq 2.4$), two distinct states are observed: the $\mathcal{PS}$ and $\mathcal{PB}$ states. Both states resemble the $\mathcal{B}$ state, featuring two, antipodal disclination lines and a central smectic domain. The difference between these states lies in the adsorption of the disclination lines to the boundary, which varies with the rod anchoring. In the $\mathcal{PS}$ state, the disclination lines are each adsorbed at approximately a single point on the boundary, as illustrated in Fig. 3A, Pinned Splay. Along the boundary, there is planar anchoring on either side of each red disclination line. On the other hand, the $\mathcal{PB}$ state has linear portions of the disclinations adsorbed, as illustrated in Fig. 3A, Pinned Bend. The increased homeotropic anchoring at the boundary causes larger portions of the red disclination line to be absorbed to the boundary. The $\mathcal{PS}$ state requires the director, which describes

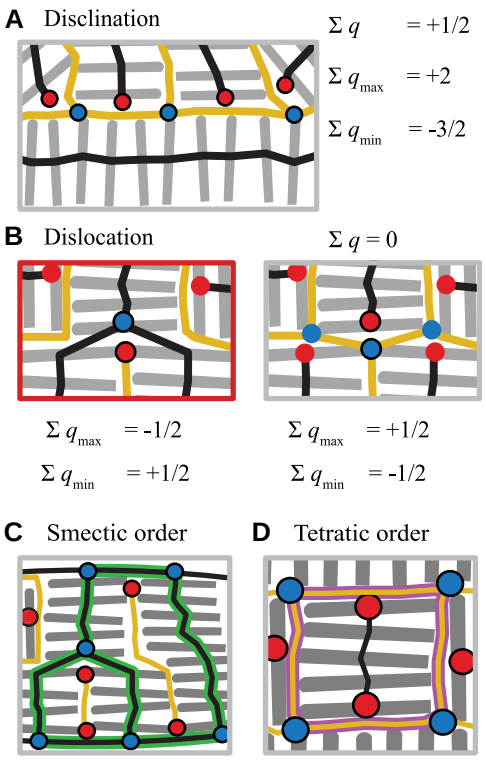

Fig. 4. Network topology associated with (A) disclinations and (B) dislocations. A) Disclinations produce positive charge in the maximum density network and negative charge for the minimum density network and have total charge of $\sum q = +1/2$. B) Dislocations have a degeneracy in the assignment of network charges. They can be represented by a split/merge in either the maximum density or minimum density networks. Each operation equivalently results in a total topological charge of zero. To distinguish dislocations from disclinations using network charges, we always assign the network split/merge to the maximum density network, highlighted by the red box (left). Schematics showing C) closed loops of the maximum density network corresponding to well-organized smectic-layers and D) closed loops of the minimum density network corresponding to tetratic regions.

the rod orientation, to splay at the point of disclination adsorption. In the $\mathcal{PB}$ state, the smectic lamellae follow the curvature of the boundary and are bent without director distortion.

We attribute the rarity of the $\mathcal{PS}$ state to differences in elastic energy contributions of director splay and layer bend for the elastic constant K in Eq. 1 for hard-rod smectics. Wensink and Grelet explored these differences in the elastic response of hard-rod smectics with a recent work that connects microscopic theory to mesoscale elasticity (51). By extending the work of Straley (81) to smectics, they find that the elastic modulus for smectic layer bending is typically two orders of magnitude lower than that of splay in the director for hard-rod smectics. Therefore, the elastic constant K in Eq. 1 is dominated by director splay deformations. In other words, for colloidal smectics, layer bending without director splay has a minimal elastic energy penalty, making the $\mathcal{PB}$ state more energetically preferred than the $\mathcal{PS}$ state.

Finally, in the case of extreme confinements ($r_1/L \leq 1.2$), the $\mathcal{V}$ state is observed, characterized by the absence of disclinations in the bulk from increased homeotropic anchoring at the ellipse vertices (labeled by red lines at the boundary in Fig. 3A, Virtual). Additionally, in certain confinements of intermediate size and eccentricity, composite states $\mathcal{C}$ are observed. We denoted which states are part of the composite using super- and subscripts: for example, a composite structure of $\mathcal{B}$ and $\mathcal{PS}$ is denoted $\mathcal{C}_{\mathcal{B}}^{\mathcal{PS}}$.

The disclination structure depends on the confinement geometry (r_1/r_2 and r_1/L) and thus the imposed anchoring. To visualize this dependence, we plot the disclination state with varying r_1/r_2 and r_1/L in Fig. 3B. In certain cases, the disclination state varies between samples or relaxes over time, for which the ratio of observed structures is plotted.

At high eccentricity and confinement, we observe the $\mathcal{V}$ state (bottom left of Fig. 3B and C). With larger confinements and decreasing eccentricity, the system configuration moves through the $\mathcal{PB}/\mathcal{PS}$ states and ends with the $\mathcal{B}$ state at the largest and most circular confinements (top right of Fig. 3B and C). Similar to the plots in Fig. 2A and B, R_{min} becomes greater with increasing r_1/L and r_1/r_2 and is colored from red ($R_{min}/L \leq 0.5$) to yellow ($0.5 < R_{min}/L \leq 1$) to blue ($R_{min}/L > 1$). The increase in R_{min} begins to alter the anchoring condition from homeotropic to planar near $R^*_{curv}/L \approx 1$. The anchoring change directly affects the disclination states. The homeotropic-to-planar anchoring transition that arises with reduced boundary curvature produces disclinations ($\mathcal{V}$ state transitions to $\mathcal{PB}/\mathcal{PS}$ states across $R_{min}/L = 0.5$ from red to yellow regions) and de-pins them from the boundary at $R_{min}/L > R^*_{curv}/L = 1$ (blue regions), pushing the disclinations into the bulk ($\mathcal{B}$ state).

The disclination state of a colloidal smectic is directly related to the dependence of anchoring on confinement curvature. Here, we explicitly establish the connection between curvature, anchoring, and disclination pinning to a surface. The anchoring condition of a colloidal liquid crystal, which is controlled by the confinement curvature, ultimately determines the disclination state.

Network analysis

We have thus far established the connection between confinement geometry, anchoring, and disclinations—defects in the orientational order marked by low values in P_2. However, smectics also exhibit positional order and, consequently, dislocation defects. Identifying dislocations requires a method that reflects the broken translational symmetry of the smectic phase. Therefore, in order to analyze the effect of confinement geometry on 2D, edge dislocations, we leverage the single-rod resolution of our system to construct networks of minimum and maximum density using an analysis method recently introduced by Monderkamp *et al.* (46).

Briefly, each network consists of a set of vertex points identifying either rod centers or rod ends, from which a network is constructed by employing a Delaunay triangulation on all these points. The boundary can be arbitrarily assigned to either the minimum density (rod ends) or maximum density network (rod centers). Here, we choose to always assign the boundary to the maximum density network. Next, the minimum and maximum density networks are separated, and empty loops are collapsed to single vertex points or lines. This process yields two interwoven yet distinct networks representing minimum (yellow lines, Fig. 4) and maximum (black lines, Fig. 4) density, respectively. We exclude interstitials from our analysis. A detailed protocol is available in the Supplementary Material (see Fig. S4).

The maximum and minimum density networks possess topological charge. The total topological charge of a network $\sum q$ can be determined by summing the charges of every vertex point on the network, where the charge q is set by the number of adjacent connected points d: $q = 1 - d/2$. In the case of the elliptical confinement, where the boundary is assigned to either the minimum or maximum density network, the system follows the Poincaré–Hopf theorem with $\sum q = \chi = +1$. Further discussion on the

topological charge conservation can be found in the recent work of Monderkamp *et al.* (46).

However, in addition to topological charge conservation, we identify features within the networks that uniquely distinguish topological defect types. In this context, we show how vertex charges and loops in the network can be used to quantify the presence of disclinations and dislocations, and to identify local tetratic order. Subsequently, we leverage these network features to examine how the confinement geometry influences the occurrence of dislocations and the formation of metastable tetratic domains.

The topological charges assigned to vertices on the minimum and maximum density networks enable the identification of disclinations as well as dislocations, shown also in a recent study conducted simultaneously by Wittmann (82). In Fig. 4, we show schematics of a disclination (Fig. 4A) and a dislocation (Fig. 4B), with the maximum density networks depicted in black and the minimum density networks in yellow. Positively charged vertices are denoted by red dots, while negatively charged vertices are represented by blue dots.

In the vicinity of a disclination, the maximum density network gains positive charges, while the minimum density network acquires negative charges. Regions with a discontinuous change in rod orientation result in the maximum density network ending at a single point, yielding a positive charge, and the minimum density network branching, forming a negative charge. The number of positive vertices on the maximum density network (or similarly, negative vertices on the minimum density network) quantifies the amount of disclinations in a system. Disclination lines exhibit an excess topological charge of +1/2 in the network, as shown in Fig. 4A. This is reflected in how the $\mathcal{B}$, $\mathcal{PS}$, and $\mathcal{PB}$ states are made up of two disclinations (Fig. 3), resulting in a total charge of +1, as expected from the Poincaré–Hopf theorem.

On the other hand, for dislocations, the network charges from both the minimum and maximum density networks total to zero, as illustrated in Fig. 4B. A smectic dislocation is characterized by either a splitting of one layer into two, or likewise a merging of two layers into one, resulting in a discontinuity in the positional order. That a dislocation in smectics can be viewed as either a merger or a branching of layers is reflected in how the minimum and maximum density networks are drawn. We demonstrate the ambiguity in the network representation of dislocations in Fig. 4B. The change in layer number from a disclination can be equally represented in the network as either branching in the maximum density network (Fig. 4B, left) or equivalently, branching in the minimum density network (Fig. 4B, right). To allow for a quantitative distinction between disclinations and dislocations using network charges, we choose to consistently represent a dislocation by branching the *maximum* density network. With this convention, negative vertices in the internal, maximum density network uniquely identify dislocations. The amount of negative charge in the maximum density network then serves as a measure for the quantity of dislocations.

However, beyond the network vertices, loops in the network analysis can further identify system features. We show for the first time that loops in maximum and minimum density networks can be used to distinguish smectic versus tetratic ordering, respectively. With our rods having an aspect ratio ~8, our system supports metastable, quasi-tetratic order, in addition to smectic order. Local tetratic regions are surrounded on all sides by disclinations and possess a net-zero topological charge. Charges in the density networks alone cannot discriminate between tetratic regions and other defects that arise with smectic order. Instead, we examine closed loops in the network to quantify the degree of tetratic and smectic order. As shown in Fig. 4C, closed maximum density loops capture smectic order by representing either two adjacent smectic layers that stretch across the confinement or a smectic dislocation. Conversely, as illustrated in Fig. 4D, closed minimum density loops capture tetratic order by enclosing a local region with rods differing in orientation by $\pi/2$ compared to their surroundings.

To quantify the amount of disclinations and dislocations with varying confinement geometry, we separately plot the total internal positive and negative charges on the *maximum* density network, $\sum q^{+/-}_{\max}$, for r_1/r_2 varying from 0.2 to 1.0 against the system size in Fig. 5A and B. The system size is measured by the confinement area A normalized by the area A_p of a single rod: $\widetilde{A} = A/A_p$. The total positive charges $\sum q^{+}_{\max}$ quantify the extent of disclinations in the system, while the total negative charges $\sum q^{-}_{\max}$ quantify the number of dislocations. Experimental data is plotted with solid symbols, while simulation data is plotted with open symbols. In general, the plots of Fig. 5A show that $\sum q^{+}_{\max}$ and $\sum q^{-}_{\max}$ both increase with system size and scale with the area. Normalizing these quantities with $\widetilde{A}$ reveals a flat distribution at larger system sizes, indicating that the defect amounts grow with the system size.

We focus first on intermediate system areas, where boundary effects dominate over bulk effects. Starting with disclinations and $\sum q^{+}_{\max}$ in Fig. 5A, we see confinements with high eccentricity ($r_1/r_2 \leq 0.4$) producing fewer positive charges in both experiments and simulations. This result agrees with our findings in Fig. 3, where higher eccentricity with decreasing r_1/r_2 leads to boundary-adsorbed disclinations ($\mathcal{PS}$ and $\mathcal{PB}$ states) that disappear in the $\mathcal{V}$ state with smaller systems. Increasing the confinement eccentricity enhances homeotropic anchoring near the ellipse vertices, resulting in fewer/shorter disclinations in the bulk. Fig. 5C exemplifies the decrease in positive internal vertices, signifying a reduction in disclination amount with increased eccentricity.

Turning towards dislocations and $\sum q^{-}_{\max}$ in Fig. 5B, we now see major differences between experiments and simulations. Experiments show a larger amount of dislocations across the varying confinement geometries compared to simulations. We attribute this disparity in dislocation number to the polydispersity in the rods used in experiments, a factor absent in simulations. In Fig. S5, we detail how the incorporation of polydispersity in simulations leads to increased magnitudes of $\sum q^{-}_{\max}$ and a higher occurrence of dislocations. Rods with lengths deviating from the average layer spacing induce shifts in the smectic layering, resulting in the formation of dislocations.

Despite differences between experiments and simulations, the data consistently shows that confinement geometry generally affects the formation of dislocations in confined smectics and most significantly at intermediate system areas. Confinements with a higher eccentricity ($r_1/r_2 \leq 0.4$) possess a higher negative internal charge, $\sum q^{-}_{\max}$, showing an increase in dislocations. In experiments, confinements with $r_1/r_2 = 0.2$ exhibit a higher amount of dislocations compared to other confining geometries, while in simulations, $r_1/r_2 = 0.2$, 0.4, and 0.6 all have more dislocations than more circular confinements. As shown by the examples in Fig. 5C, more elliptical confinements exhibit large smectic domains that can support dislocation formation, while more circular confinements exhibit almost no dislocations and feature multiple domains separated by disclinations.

The large smectic domain in confinements with high eccentricity supports the creation of dislocations due to boundary curvature. Consider a confinement ellipse with $r_1/r_2 = 0.2$ and $r_1/L = 2.45$. Using the boundary charges from the network analysis (Fig. S6), we determine the average smectic layer spacing λ to be

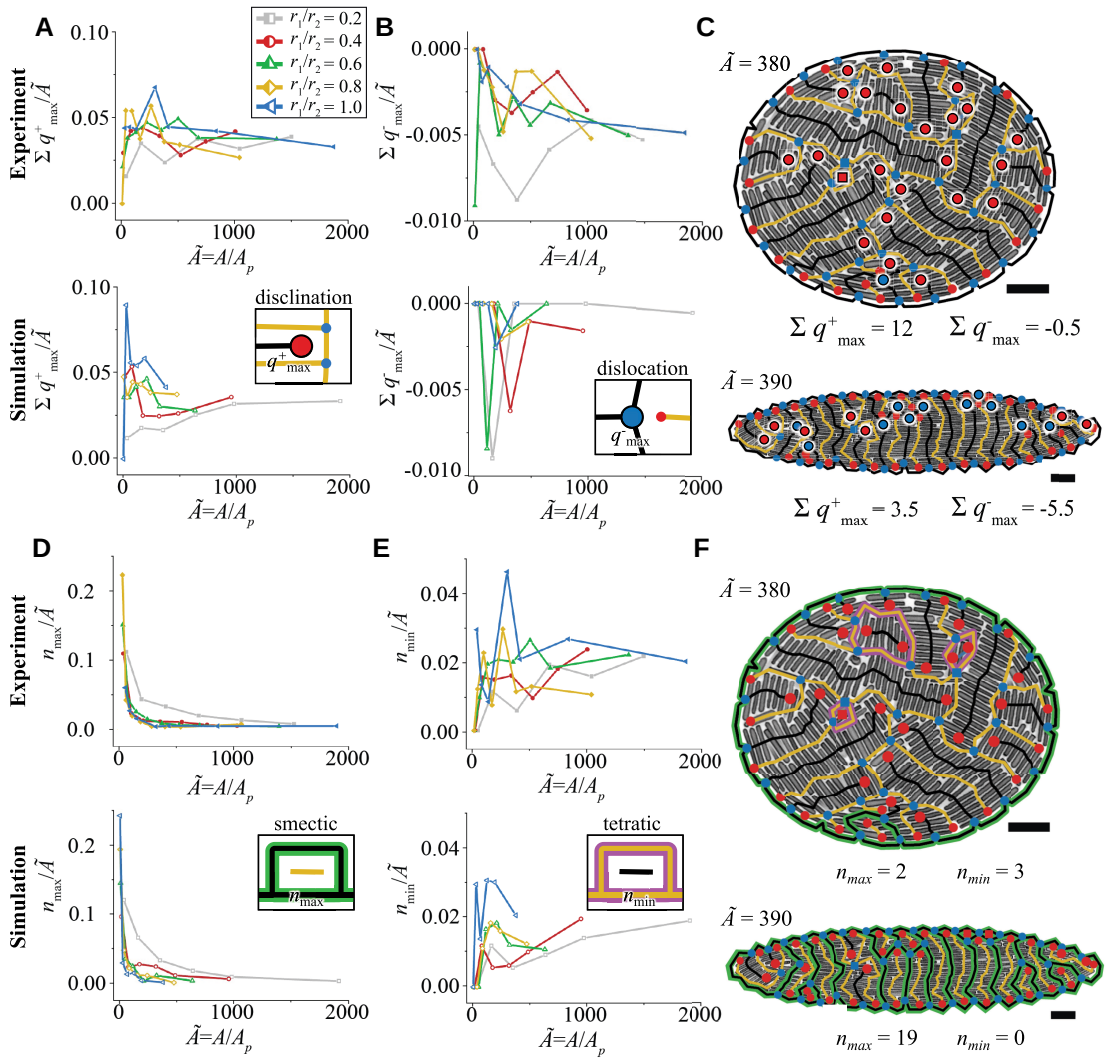

Fig. 5. Plotting network features for different confinement shapes, represented by different colors (see legend). Experiments are filled data symbols, while simulations are open data symbols. Insets show schematic representations of network features with the corresponding defect/order type. Positive A) and negative B) network charge for the maximum density network $\sum q_{max}$, is divided by the normalized confinement area $\tilde{A} = A/A_p$, where A denotes the confinement area and A_p the particle area. $\sum q_{max}/\tilde{A}$ is then plotted against $\tilde{A}$. Positive maximum density network charge $\sum q^+_{max}$ is associated with disclinations, while negative maximum network charge $\sum q^-_{max}$ is associated with dislocations. Varying confinement shapes (r_1/r_2) are plotted in different colors, shown in the legend (A, top). The number of maximum density loops n_{max} D) and minimum density loops n_{min} E) is divided by the normalized confinement area $\tilde{A} = A/A_p$, where A denotes the confinement area and A_p the particle area. $n/\tilde{A}$ is then plotted against $\tilde{A}$. Maximum density network loops are associated with ordered smectic layers, while minimum density network loops are associated with tetratic regions. Experiment snapshots for $r_1/r_2 = 0.8$, $r_1/L = 3.6$ C and F, top) and $r_1/r_2 = 0.2$, $r_1/L = 1.9$ C and F, bottom) demonstrate that, for comparable $\tilde{A}$, the confinement with higher eccentricity has fewer internal q^+_{max} (C, highlighted red dots), indicating disclination suppression, as well as more internal q^-_{max} (C, highlighted blue dots), indicating dislocation promotion. Likewise, for comparable $\tilde{A}$, the confinement with higher eccentricity has more maximum density loops (F, green loops), indicating high smectic order, as well as fewer minimum density loops (F, purple loops), indicating low tetratic order. Scale bars are 10 μm.

$\lambda = 1.1L$. The number of layers m that can fit across the center of the ellipse is $m_{center} = 2r_2/\lambda = 22.3$. On the other hand, the number of layers that can fit along the bottom of the confinement is $m_{bottom} = C/(2\lambda) = 23.4$, where C is the confinement circumference. The incommensurate number of layers from the center to the boundary leads to geometrical frustration that is relieved by the Helfrich–Hurault instability (40), which nucleates dislocations. The combination of long-range smectic order, the incommensurate number of layers from the curved boundary, and the rod polydispersity collectively contribute to the prevalence of dislocations in highly elliptical confinements.

Loops in the maximum and minimum density networks serve to further identify and quantify the degree of smectic and tetratic order. In Fig. 5D, we plot the number of loops in the maximum density network, n_{max}, for both experiments and simulations. Confining geometries with high eccentricity, specifically $r_1/r_2 = 0.2$, exhibit larger values of n_{max} compared to more circular confinements, most notably at intermediate system areas. A system with an intermediate, normalized area $\tilde{A} = 390$ is shown at the bottom of Fig. 5F, where maximum density loops are highlighted in green. Higher n_{max} values corroborate that high confinement eccentricity facilitates smectic order.

At intermediate system areas, confinements with higher eccentricity also exhibit lower n_{min} values and thereby less tetratic order than more circular confinements, consistent with confinement ellipticity promoting smectic order. Fig. 5F highlights confinement geometries with r_1/r_2 of 0.2 and 0.6, both with comparable areas, $\tilde{A} = 390$ and 380, respectively. The more circular confinement

(Fig. 5F, top) has $n_{min} = 3$, reflecting three local, quasi-tetratic regions. In contrast, the more elliptical confinement (Fig. 5F, bottom) has no tetratic regions, with $n_{min} = 0$.

However, the ability of the boundary to influence the bulk order is limited by the system size. At larger areas, both $\sum q^{+}_{max}$ and $\sum q^{-}_{max}$ scale with the area with no discernible trend with confinement shape, r_1/r_2. Furthermore, for larger systems, n_{max} starts to scale linearly with area, due to the emergence of metastable, tetratic order in the bulk. The appearance of local, quasi-tetratic regions in larger systems stems from the anchoring extrapolation length limiting the extent of order that a surface can impose into the bulk (40, 83–85). These quasi-tetratic regions introduce disclinations that disrupt the formation of maximum density loops, shown in Fig. 5D for $r_1/r_2 = 0.2$, where n_{max} approaches values observed in more circular systems. Circular confinements form disclinations due to the confinement shape promoting planar anchoring, which disrupts the smectic order. An unconfined system also forms disclinations due to metastable, short-ranged, and quasi-tetratic order. Therefore, when elliptical systems with $r_1/r_2 = 0.2$ become sufficiently large, the bulk contains more disclinations due to the formation of localized, tetratic regions. The anchoring from the elliptical confinement can only suppress metastable, tetratic order in the vicinity of the boundary, within a distance set by the anchoring extrapolation length. The increase of quasi-tetratic order for $r_1/r_2 = 0.2$ with large areas is also evident in the number of loops in the minimum density network, n_{min}, as plotted in Fig. 5E. n_{min} positively scales with the system area with no discernible effect of confinement shape at large areas, which is once again a consequence of the anchoring extrapolation length. Upon increasing the system size, the liquid crystal has more available bulk area, allowing for the formation of metastable, tetratic structures.

Our network charge analysis enables the quantification of dislocations. Dislocations form in confinements with high eccentricity, due to homeotropic anchoring in high curvature regions creating long-ranged smectic order. Closed network loops distinguish smectic from tetratic order. Confinements with high eccentricity suppress metastable, tetratic order. The anchoring conditions formed by ellipses with high regions of curvature can be leveraged to curb metastable structures, yielding long-range order.

Conclusion

To sum up, we have demonstrated using both experiments and simulations that the anchoring and defect state of confined colloidal smectics are directed by boundary curvature. By varying the size and shape of elliptical confinements, we effectively tune the local boundary curvature. The transition from planar to homeotropic anchoring is found to occur at a local, critical radius of curvature, approximately twice the rod length, $R^{*}_{curv} \approx 2L$, a robust quantity that holds across a broad range of rod aspect ratios and packing fractions. Being a *local* geometric quantity, we anticipate our finding to influence the future design of boundaries for anchoring control, beyond the enclosed confinements used in the present study. For instance, local curvature can be patterned topographically along long walls and channels to achieve entropic, homeotropic anchoring over a large surface. The explicit demonstration of homeotropic anchoring via designed, local curvature over a large area is the subject of a future study. We then demonstrate the use of anchoring control imposed by the local boundary curvature to set the disclination state of the confined system. We employ a network analysis to distinguish disclinations and dislocations by examining topological charges, and we further expand the analysis to include network loops in the minimum and maximum density networks to differentiate smectic and tetratic ordering. The defect types in the smectic phase can be selected by adjusting the boundary curvature: planar anchoring in confinements with large curvatures promotes disclinations, while homeotropic anchoring in highly curved, elliptical confinements favors dislocations. In ellipses of intermediate sizes, metastable structures can be suppressed when the anchoring extrapolation length covers a significant portion of the bulk, resulting in long-range smectic order.

Interestingly, both experiments and simulations consistently reveal the effect of boundary curvature on disclinations but with slight variations in the value of R^{*}_{curv} and the number of dislocations. We attribute this discrepancy to the polydispersity of rods in experiments, a factor absent in simulations. In Fig. S3 and Table S1, we use simulations to probe the possible influence of polydispersity on R^{*}_{curv}. For smectics formed at packing fraction $\phi = 0.81$, we find monodisperse rods with $L/D = 8$ yielding $R^{*}_{curv} \approx 1.58L$, while polydisperse rods give an increased critical radius of curvature of $R^{*}_{curv} \approx 1.67L$. It is therefore plausible that polydispersity is a factor for why we measure a larger R^{*}_{curv} in experiments compared to simulations. We additionally examine the effect of polydispersity on the production of dislocations across confinement geometries, shown in Fig. S5 and Table S2. We find that dislocations increase in systems with polydisperse rods. Disclinations, characterized by an excess network charge of $\sum q = +1/2$, are significantly affected by the topological frustration arising from confinement. This topological frustration is largely unaffected by rod polydispersity (see Fig. S5 and Table S2). However, dislocations have a neutral topological contribution ($\sum q = 0$) and are thereby more susceptible to local differences in microscopic interactions and macroscopic properties. Polydispersity in the rod shape and size alters the excluded-volume interactions of the rods with a hard-wall boundary, potentially impacting the rod anchoring. Additionally, polydispersity may alter macroscopic, elastic properties. In recent work connecting microscopic interactions of hard rods to mesoscale elasticity (51), Wensink and Grelet found that the positional fluctuation of rods normal to their layer leads to a reduction in the layer bending modulus K in Eq. 1. Polydispersity, leading to deviations in rod lengths from the average smectic layer size, has been shown to increase inter-layer diffusion (86). Given the significant bend deformations experienced by smectic layers around a dislocation, polydispersity in rod length could potentially lower the energy required to form a dislocation by reducing K. The effect of rod polydispersity on the mesoscale, elastic energy of lyotropic smectics remains to be fully elucidated and requires further study.

Lastly, we note an interesting observation in polydisperse, simulated systems, where rods with $L/D < 4$ sample a relatively large area of the confinement compared to longer rods, shown in Fig. S7 and Supplementary Material, Video S2. These shorter rods can group and locate in between smectic layers as interstitials. Across all confinements, the short rods can locate near the boundary as well as remain within the bulk. We also see short rods in experiments locating near boundaries (see Fig. 1D) as well as in disclinations (see Fig. 5C and F). We have removed interstitials from our analysis, but the size-selective interactions of rods near boundaries and defects is an interesting research question that requires further investigation.

To conclude, we have demonstrated the control of anchoring and defects in hard-rod smectics using only hard-wall interactions. As the rod anchoring depends solely on the local wall geometry, our findings are applicable to liquid crystalline systems across various length scales. The conclusions gained from this work help to establish design principles for the self-assembly

and defect control of larger-scaled liquid crystals, such as anisotropic cells (16–21) and nanorods (9, 25–30)—important for the development of bio- and nano-technologies.

Acknowledgments

We thank Dave van den Heuvel, Relinde van Dijk-Moes, Albert Grau Carbonell, and Roy Hoitink for experimental support. We thank Amir Raoof for access to clean-room facilities. We also thank Alfons van Blaaderen, Arnout Imhof, and Randall D. Kamien for helpful discussions.

Supplementary Material

Supplementary material is available at *PNAS Nexus* online.

Funding

E.I.L.J. acknowledges funding from the European Commission (Horizon-MSCA, Grant No. 101065631). G.C.-V. acknowledges financial support from the Nederlandse Organisatie voor Wetenschappelijk Onderzoek (NWO) ENW PPS Fund 2018-Technology Area Soft Advanced Materials (Grant No. ENPPS.TA.018.002). M.D. acknowledges financial support from the European Research Council (Grant No. ERC-2019-ADV-H2020 884902 SoftML). L.T. acknowledges support from the European Commission (Horizon-MSCA, Grant No. 892354) and the NWO ENW Veni grant (Project No. VI.Veni.212.028). E.I.L.J. and L.T. acknowledge support from the Starting PI Fund for Electron Microscopy Access from Utrecht University's Electron Microscopy Center.

Author Contributions

E.I.L.J.: conceptualization, formal analysis (equal), writing – original draft (equal), writing – review and editing, investigation, methodology, software, data curation, visualization (equal), funding acquisition; G.C.-V.: formal analysis (equal), writing – original draft (equal), writing – review and editing, investigation, methodology, software, visualization (equal); M.D.: conceptualization, formal analysis (supporting), methodology, writing – review and editing, funding acquisition, supervision; Q.T.: methodology, resources; L.T.: conceptualization (lead), formal analysis (supporting), methodology, writing – original draft (equal), writing – review and editing (lead), funding acquisition, supervision.

Preprints

This manuscript was posted on a preprint repository: https://arxiv.org/abs/2311.18362.

Data Availability

Data and code associated with this work is available from Dataverse NL at https://doi.org/10.34894/VL9FGP(89).

References

1 Chaikin PM, Lubensky TC. 1995. *Principles of condensed matter physics*. Cambridge University Press.
2 de Gennes PG, Prost J. 1993. *The physics of liquid crystals*. Oxford University Press.
3 Khoo IC, Wu ST. 1993. Optics and nonlinear optics of liquid crystals, Series in nonlinear optics. Vol. 1. World Scientific. p. 440.
4 Muševič I, Škarabot M, Tkalec U, Ravnik M, Žumer S. 2006. Two-dimensional nematic colloidal crystals self-assembled by topological defects. *Science*. 313:954–958.
5 Hegmann T, Qi H, Marx VM. 2007. Nanoparticles in liquid crystals: synthesis, self-assembly, defect formation and potential applications. *J Inorg Organomet Polym Mater*. 17:483–508.
6 Tran L, Bishop KJM. 2020. Swelling cholesteric liquid crystal shells to direct the assembly of particles at the interface. *ACS Nano*. 14:5459–5467.
7 Warner M, Terentjev EM. 2007. *Liquid crystal elastomers*. Vol. 120. Oxford University Press.
8 Ye X, *et al.* 2012. Improved size-tunable synthesis of monodisperse gold nanorods through the use of aromatic additives. *ACS Nano*. 6:2804–2817.
9 Diroll BT, Greybush NJ, Kagan CR, Murray CB. 2015. Smectic nanorod superlattices assembled on liquid subphases: structure, orientation, defects, and optical polarization. *Chem Mater*. 27:2998–3008.
10 Tebbe M, *et al.* 2015. Optically anisotropic substrates via wrinkle-assisted convective assembly of gold nanorods on macroscopic areas. *Faraday Discuss*. 181:243–260.
11 Wang T, *et al.* 2012. Self-assembled colloidal superparticles from nanorods. *Science*. 338:358–363.
12 Dell'Arciprete D, *et al.* 2018. A growing bacterial colony in two dimensions as an active nematic. *Nat Commun*. 9:4190.
13 Yaman YI, Demir E, Vetter R, Kocabas A. 2019. Emergence of active nematics in chaining bacterial biofilms. *Nat Commun*. 10:2285.
14 Copenhagen K, Alert R, Wingreen NS, Shaevitz JW. 2021. Topological defects promote layer formation in Myxococcus xanthus colonies. *Nat Phys*. 17:211–215.
15 Prasad M, *et al.* 2023. Alcanivorax borkumensis biofilms enhance oil degradation by interfacial tubulation. *Science*. 381:748–753.
16 Doostmohammadi A, Thampi SP, Yeomans JM. 2016. Defect-mediated morphologies in growing cell colonies. *Phys Rev Lett*. 117:048102.
17 Kawaguchi K, Kageyama R, Sano M. 2017. Topological defects control collective dynamics in neural progenitor cell cultures. *Nature*. 545:327–331.
18 Saw TB, *et al.* 2017. Topological defects in epithelia govern cell death and extrusion. *Nature*. 544:212–216.
19 Maroudas-Sacks Y, *et al.* 2021. Topological defects in the nematic order of actin fibres as organization centres of hydra morphogenesis. *Nat Phys*. 17:251–259.
20 Vafa F, Mahadevan L. 2022. Active nematic defects and epithelial morphogenesis. *Phys Rev Lett*. 129:098102.
21 Kaiyrbekov K, *et al.* 2023. Migration and division in cell monolayers on substrates with topological defects. *Proc Natl Acad Sci U S A*. 120:e2301197120.
22 Kleman M, Laverntovich OD. 2007. *Soft matter physics: an introduction*. Springer Science & Business Media.
23 Alexander GP, Chen BGG, Matsumoto EA, Kamien RD. 2012. Colloquium: disclination loops, point defects, and all that in nematic liquid crystals. *Rev Mod Phys*. 84:497–514.
24 Kamien RD, Santangelo CD. 2006. Smectic liquid crystals: materials with one-dimensional, periodic order. *Geom Dedicata*. 120:229–240.
25 Vroege GJ, Thies-Weesie DME, Petukhov AV, Lemaire BJ, Davidson P. 2006. Smectic liquid-crystalline order in suspensions of highly polydisperse goethite nanorods. *Adv Mater*. 18:2565–2568.

26 Querner C, Fischbein MD, Heiney PA, Drndić M. 2008. Millimeter-scale assembly of CdSe nanorods into smectic superstructures by solvent drying kinetics. *Adv Mater*. 20:2308–2314.
27 Zanella M, *et al.* 2011. Self-assembled multilayers of vertically aligned semiconductor nanorods on device-scale areas. *Adv Mater*. 23:2205–2209.
28 Hosseini SN, *et al.* 2020. Smectic liquid crystalline titanium dioxide nanorods: reducing attractions by optimizing ligand density. *Adv Funct Mater*. 30:2005491.
29 Hussain M. 2021. Liquid crystal elastomers for biological applications. *Nanomaterials*. 11(3):813.
30 Jehle F, *et al.* 2021. Collagen pentablock copolymers form smectic liquid crystals as precursors for mussel Byssus fabrication. *ACS Nano*. 15:6829–6838.
31 Lopez-Leon T, Fernandez-Nieves A, Nobili M, Blanc C. 2011. Nematic-smectic transition in spherical shells. *Phys Rev Lett*. 106:247802.
32 Liang HL, Schymura S, Rudquist P, Lagerwall J. 2011. Nematic-smectic transition under confinement in liquid crystalline colloidal shells. *Phys Rev Lett*. 106:247801.
33 Jeong J, Kim MW. 2012. Confinement-induced transition of topological defects in smectic liquid crystals: from a point to a line and pearls. *Phys Rev Lett*. 108:207802.
34 Kuijk A, Byelov DV, Petukhov AV, van Blaaderen A, Imhof A. 2012. Phase behavior of colloidal silica rods. *Faraday Discuss*. 159: 181–199.
35 Serra F, *et al.* 2015. Curvature-driven, one-step assembly of reconfigurable smectic liquid crystal "compound eye" lenses. *Adv Opt Mater*. 3:1287–1292.
36 Coursault D, *et al.* 2016. Self-organized arrays of dislocations in thin smectic liquid crystal films. *Soft Matter*. 12:678–688.
37 Gim MJ, Beller DA, Yoon DK. 2017. Morphogenesis of liquid crystal topological defects during the nematic-smectic a phase transition. *Nat Commun*. 8:15453.
38 Cortes LBG, Gao Y, Dullens RPA, Aarts DGAL. 2017. Colloidal liquid crystals in square confinement: isotropic, nematic and smectic phases. *J Phys: Condens Matter*. 29:064003.
39 Repula A, Grelet E. 2018. Elementary edge and screw dislocations visualized at the lattice periodicity level in the smectic phase of colloidal rods. *Phys Rev Lett*. 121:097801.
40 Blanc C, *et al.* 2023. Helfrich-Hurault elastic instabilities driven by geometrical frustration. *Rev Mod Phys*. 95:015004.
41 Chen BGG, Alexander GP, Kamien RD. 2009. Symmetry breaking in smectics and surface models of their singularities. *Proc Natl Acad Sci U S A*. 106:15577–15582.
42 Kamien RD, Mosna RA. 2016. The topology of dislocations in smectic liquid crystals. *New J Phys*. 18:053012.
43 Aharoni H, Machon T, Kamien RD. 2017. Composite dislocations in smectic liquid crystals. *Phys Rev Lett*. 118:257801.
44 Monderkamp PA, *et al.* 2021. Topology of orientational defects in confined smectic liquid crystals. *Phys Rev Lett*. 127:198001.
45 Hocking BJ, Ansell HS, Kamien RD, Machon T. 2022. The topological origin of the Peierls–Nabarro barrier. *Proc R Soc A: Math Phys Eng Sci*. 478:20210725.
46 Monderkamp PA, Windisch RS, Wittmann R, Löwen H. 2023. Network topology of interlocked chiral particles. *J Chem Phys*. 158:164505.
47 Severino PG, Kamien RD. 2024. Escape from the second dimension: a topological distinction between edge and screw dislocations. *Phys Rev E*. 109:L012701.
48 Pevnyi MY, Selinger JV, Sluckin TJ. 2014. Modeling smectic layers in confined geometries: order parameter and defects. *Phys Rev E*. 90:032507.
49 Xia J, MacLachlan S, Atherton TJ, Farrell PE. 2021. Structural landscapes in geometrically frustrated smectics. *Phys Rev Lett*. 126:177801.
50 Paget J, Mazza MG, Archer AJ, Shendruk TN. 2023. Complex-tensor theory of simple smectics. *Nat Commun*. 14:1048.
51 Wensink HH, Grelet E. 2023. Elastic response of colloidal smectic liquid crystals: insight from microscopic theory. *Phys Rev E*. 107: 054604.
52 Frenkel D, Lekkerkerker HNW, Stroobants A. 1988. Thermodynamic stability of a smectic phase in a system of hard rods. *Nature*. 332:822–823.
53 Poniewierski A, Hołyst R. 1988. Density-functional theory for nematic and Smectic—*a* ordering of hard spherocylinders. *Phys Rev Lett*. 61:2461–2464.
54 van Roij R, Bolhuis P, Mulder B, Frenkel D. 1995. Transverse interlayer order in lyotropic smectic liquid crystals. *Phys Rev E*. 52: R1277–R1280.
55 Graf H, Löwen H. 1999. Phase diagram of tobacco mosaic virus solutions. *Phys Rev E*. 59:1932–1942.
56 Savenko SV, Dijkstra M. 2004. Sedimentation and multiphase equilibria in suspensions of colloidal hard rods. *Phys Rev E*. 70: 051401.
57 Wen X, Meyer RB, Caspar DLD. 1989. Observation of smectic-a ordering in a solution of rigid-rod-like particles. *Phys Rev Lett*. 63: 2760–2763.
58 Grelet E. 2014. Hard-rod behavior in dense mesophases of semiflexible and rigid charged viruses. *Phys Rev X*. 4:021053.
59 Kuijk A, *et al.* 2014. Effect of external electric fields on the phase behavior of colloidal silica rods. *Soft Matter*. 10:6249–6255.
60 de las Heras D, Velasco E, Mederos L. 2006. Capillary effects in a confined smectic phase of hard spherocylinders: influence of particle elongation. *Phys Rev E*. 74:0011709.
61 Geigenfeind T, Rosenzweig S, Schmidt M, de las Heras D. 2015. Confinement of two-dimensional rods in slit pores and square cavities. *J Chen Phys*. 142:174701.
62 de las Heras D, Velasco E. 2014. Domain walls in two-dimensional nematics confined in a small circular cavity. *Soft Matter*. 10:1758.
63 González-Pinto M, Borondo F, Martinez-Ratón Y, Velasco E. 2017. Clustering in vibrated monolayers of granular rods. *Soft Matter*. 13:2571.
64 Wittmannm R, Cortes LBG, Löwen H, Aarts DGAL. 2021. Particle-resolved topological defects of smectic colloidal liquid crystals in extreme confinement. *Nat Commun*. 12:623.
65 Armas ADD, Maza-cuello M, Martínez-Ratón Y, Velasco E. 2020. Domain walls in vertically vibrated monolayers of cylinders confined in annuli. *Phys Rev Res*. 2:033436.
66 Wittmann R, *et al.* 2023. Colloidal smectics in button-like confinements: Experiment and theory. *Phys Rev Res*. 5:033135.
67 Frka-Petesic B, *et al.* 2023. Structural color from cellulose nanocrystals or chitin nanocrystals: self-assembly, optics, and applications. *Chem Rev*. 123:12595–12756.
68 Jerome B. 1991. Surface effects and anchoring in liquid crystals. *Rep Prog Phys*. 54:391.
69 Allen MP. 1999. Molecular simulation and theory of liquid crystal surface anchoring. *Mol Phys*. 96:1391–1397.
70 Rodríguez-Ponce I, Romero-Enrique JM, Velasco E, Mederos L, Rull LF. 1999. Interplay between anchoring and wetting at a nematic-substrate interface. *Phys Rev Lett*. 82:2697–2700.
71 Dijkstra M, van Roij R, Evans R. 2001. Wetting and capillary nematization of a hard-rod fluid: a simulation study. *Phys Rev E*. 63:051703.
72 Barmes F, Cleaver DJ. 2004. Computer simulation of a liquid-crystal anchoring transition. *Phys Rev E*. 69:061705.

73 de las Heras D, Velasco E, Mederos L. 2005. Capillary smectization and layering in a confined liquid crystal. *Phys Rev Lett*. 94:017801.
74 Basurto E, Gurin P, Varga S, Odriozola G. 2020. Ordering, clustering, and wetting of hard rods in extreme confinement. *Phys Rev Res*. 2:013356.
75 Cosentino Lagomarsino M, Dogterom M, Dijkstra M. 2003. Isotropic–nematic transition of long, thin, hard spherocylinders confined in a quasi-two-dimensional planar geometry. *J Chem Phys*. 119:3535–3540.
76 Lewis AH, *et al*. 2014. Collloidal liquid crystals in rectangular confinement: theory and experiment. *Soft Matter*. 10:7865.
77 Gârlea IC, *et al*. 2016. Finite particle size drives defect-mediated domain structures in strongly confined colloidal liquid crystals. *Nat Commun*. 7:12112.
78 Pratley VJ, Caf E, Ravnik M, Alexander GP. 2024. Three-dimensional spontaneous flow transition in a homeotropic active nematic. *Commun Phys*. 7:127.
79 Bates MA, Frenkel D. 2000. Phase behavior of two-dimensional hard rod fluids. *J Chem Phys*. 112:10034.
80 Ni R, Belli S, van Roij R, Dijkstra M. 2010. Glassy dynamics, spinodal fluctuations, and the kinetic limit of nucleation in suspensions of colloidal hard rods. *Phys Rev Lett*. 105:088302.
81 Straley JP. 1976. Theory of piezoelectricity in nematic liquid crystals, and of the cholesteric ordering. *Phys Rev A*. 14:1835–1841.
82 Wittmann R. 2024. Layer topology of smectic grain boundaries. *Liq Cryst*. 1–7.
83 Kralj S, Žumer S. 1996. Smectic-a structures in submicrometer cylindrical cavities. *Phys Rev E*. 54:1610–1617.
84 Vaupotič N, Kralj S, Čopič M, Sluckin TJ. 1996. Landau–de Gennes theory of the chevron structure in a smectic liquid crystal. *Phys Rev E*. 54:3783–3792.
85 Kutnjak Z, Kralj S, Lahajnar G, Žumer S. 2004. Influence of finite size and wetting on nematic and smectic phase behavior of liquid crystal confined to controlled-pore matrices. *Phys Rev E*. 70:051703.
86 Chiappini M, Grelet E, Dijkstra M. 2020. Speeding up dynamics by tuning the noncommensurate size of rodlike particles in a smectic phase. *Phys Rev Lett*. 124:087801.
87 Poincaré H. 1881. Mémoire sur les courbes définies par une équation différentielle (i). *J de Mathématiques Pures et Appliquées 3^{e} Série*. 7:375–422.
88 Hopf H. 1927. Vektorfelder in n-dimensionalen mannigfaltigkeiten. *Math Ann*. 96:225–249.
89 Jull EIL, Campos-Villalobos G, Tang Q, Dijkstra M, Tran L. 2024. Dataset associated with "Curvature directed anchoring and defect structure of colloidal smectic liquid crystals in confinement". *DataverseNL* V1, https://doi.org/10.34894/VL9FGP.